Dirac cones in isogonal hexagonal metallic structures

Kang Wang*
Laboratoire de Physique des Solides, UMR CNRS/Université Paris-Sud, Université Paris-Saclay, 91405 Orsay, France

(Received 29 December 2017; revised manuscript received 14 March 2018; published 26 March 2018)

A honeycomb hexagonal metallic lattice is equivalent to a triangular atomic one and cannot create Dirac cones in its electromagnetic wave spectrum. We study in this work the low-frequency electromagnetic band structures in isogonal hexagonal metallic lattices that are directly related to the honeycomb one and show that such structures can create Dirac cones. The band formation can be described by a tight-binding model that allows investigating, in terms of correlations between local resonance modes, the condition for the Dirac cones and the consequence of the third structure tile sustaining an extra resonance mode in the unit cell that induces band shifts and thus nonlinear deformation of the Dirac cones following the wave vectors departing from the Dirac points. We show further that, under structure deformation, the deformations of the Dirac cones result from two different correlation mechanisms, both reinforced by the lattice's metallic nature, which directly affects the resonance mode correlations. The isogonal structures provide new degrees of freedom for tuning the Dirac cones, allowing adjustment of the cone shape by modulating the structure tiles at the local scale without modifying the lattice periodicity and symmetry.

DOI: 10.1103/PhysRevB.97.125146

I. INTRODUCTION

Artificial graphenes mimic the electronic band structures of atomic lattices by creating Dirac conical singularities in their dispersion relations [1]. Many such systems, involving various mechanisms, have been reported, including semiconductor [2] and molecular [3] honeycomb structures confining two-dimensional electron gases, cold atoms trapped in honeycomb optical lattices [4,5], polaritons excited in a honeycomb lattice of coupled micropillars [6], photon-phonon polaritons excited on a honeycomb lattice in an optomechanical crystal [7], photonic crystals of hexagonal [8] and honeycomb [9] dielectric structures, honeycomb arrays of solid [10] and hollow [11] cylinders controlling acoustic waves propagations, etc. Collective plasmon modes in honeycomb lattices of metallic particles have also been proposed [12,13]. Artificial graphenes enable us to probe Dirac-cone-related physical properties inaccessible in atomic structures, allowing structure configurations and modulations difficult to realize in the latter, and have potential application in material design. As one class of such systems, photonic crystals can be coupled to the electromagnetic (EM) emissions and affect their dispersion relations, allowing us to optically probe the properties of Dirac cones. Various phenomena have been studied, such as conical diffraction, gap solitons, pseudodiffusive transmission, the quantum Hall-like effect, and the zero refractive index [14–17].

Dirac cones can emerge in triangular [15,16,18], honeycomb [14,15], and square [17] lattices in dielectric photonic structure, where the cone formation can be described by a nearly-free-photon approximation [8]. Concerning the metallic photonic structures, Dirac cones have been, until now, found in triangular lattices [19,20] rather than in the honeycomb one. In fact, a honeycomb metallic lattice is equivalent to a triangular atomic one. Indeed, in a metallic lattice, the low-frequency EM frequency bands are formed by local resonance modes confined inside the structure tiles [21,22]. For a honeycomb lattice, the local resonance modes follow the dual triangular distribution and cannot create Dirac cones. However, for a triangular lattice, the local resonance modes can be formed inside the triangular tiles [20] and thus follow the dual honeycomb distribution. Such a lattice is equivalent to a honeycomb atomic one, and Dirac cones can emerge.

A honeycomb lattice can be modulated to form isogonal hexagonal tilings [23] that contain two kinds of tiles, i.e., regular and isogonal hexagons, without changing the lattice hexagonal symmetry. In this work we study the low-frequency EM band structures in isogonal hexagonal metallic lattices and show that such structures can create Dirac cones. We explore, in the framework of a tight-binding (TB) model, the condition of the Dirac cones in the presence of a third structure tile in the unit cell in terms of the local resonance modes and their mutual correlations and investigate the deformation induced by the third mode in band structures departing from the Dirac point. We discuss the band evolution following the structure deformation and show that the Dirac cone undergoes deformations through two ways; both are related to the anisotropy in the correlations, reinforced by the lattice's metallic nature. Finally, we discuss the consequences of various parameters controlling the band structures in the vicinity of the Dirac point and show that it is possible to adjust the Dirac cone shape by modulating the relative sizes of the two kinds of tiles.

II. LOW-FREQUENCY BAND STRUCTURES

A. Structures and tiles

An isogonal hexagonal structure with unit-cell size a is displayed in Fig. 1; it belongs to the symmetry group D_6

*kang.wang@u-psud.fr

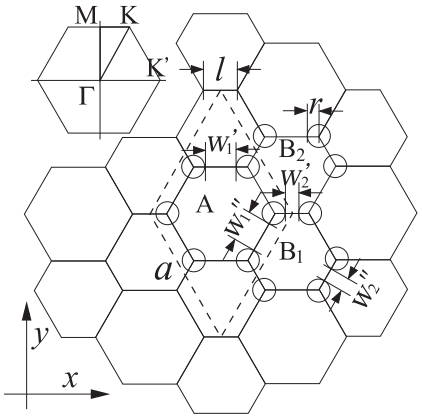

FIG. 1. An isogonal hexagonal tiling, constructed by tiles A and B (B_1 and B_2). The unit cell, with parameter a, is delimited by dashed lines. The relative sizes of these tiles, as well as the shapes of the B tiles, can be modulated by varying l without changing a.

and is constructed by two kinds of tiles. The A tiles are regular hexagons, whiles the B tiles (denoted by B_1 and B_2 for opposite orientations) are isogonal hexagons. By adjusting the common edge length between two neighboring isogonal hexagons, we can modulate the lattice pattern at the local scale without changing the lattice periodicity and symmetry group. Considering the edge length l between the tiles B_1 and B_2, for $l = a/3$, all the tiles are regular hexagons, and we have a hexagonal honeycomb tiling. Otherwise, the lattice remains an isogonal tiling as long as $a > l > 0$. As a matter of fact, it corresponds to the IG 92 tiling in the classification of Ref. [23]. Metallic cylinders, with radius r and the dielectric constant set to negative infinity, are placed at the lattice nodes in an air background to form the metallic lattices. The radius r is chosen as one tenth of the hexagon's long diagonal when $l = a/3$, i.e., $r = a/15$, corresponding to a filling rate of 9.67%.

The tiles are physically delimited by the metallic cylinders at the vertices and show a cavitylike effect by confining TM-polarized (electrical field perpendicular to the lattice plane) EM resonance modes inside. Figure 2 displays the lowest-frequency modes formed inside A and B_1 tiles for $l = 0.31a$, obtained by solving Maxwell's equations for individual tiles using the finite-difference time-domain (FDTD) method. These modes have an electrical-field maximum at the tile center, with eigenfrequencies ω_A and $\omega_{B1} = 1.1959$ and $1.2781[\omega a/(2\pi c)]$ and quality factors Q_A and $Q_{B1} = 128.3$ and 142.5.

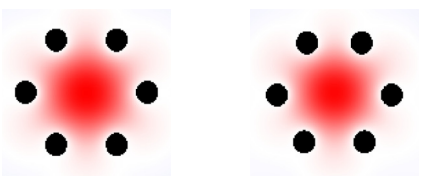

(a) (b)

FIG. 2. Electric-field distributions of the lowest-frequency TM resonance modes formed inside individual (a) A and (b) B_1 tiles for $l = 0.31a$.

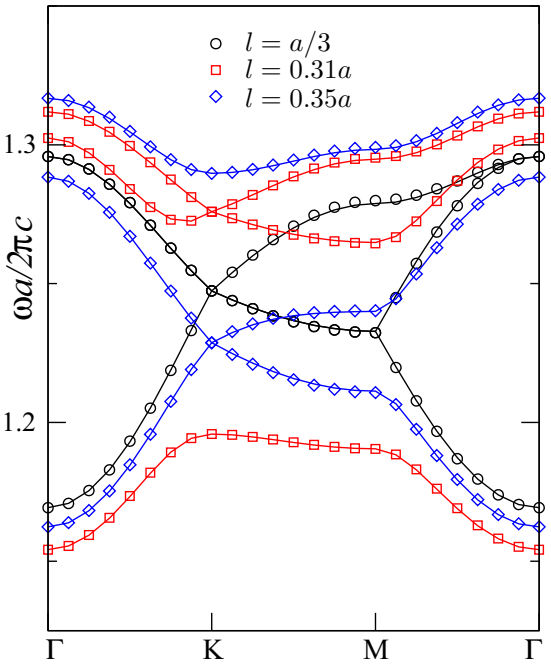

FIG. 3. Diagrams of the first three bands for $l = a/3$, $0.31a$, and $0.35a$. The FDTD solutions are represented by various symbols, while those obtained with the tight-binding model are shown by solid lines.

B. Numerical solutions

The EM frequency band diagrams for the first three bands for the TM polarization are obtained by solving Maxwell's equations using the FDTD method and are displayed in Fig. 3. Three l lengths, $l = a/3$, $0.31a$, and $0.35a$, are considered.

For $l = a/3$, the three band branches result from the folding of a single band since the unit cell is a supercell containing three identical hexagons in this configuration. The degeneracy is partially lifted for $l \neq a/3$, and the Dirac point K_D is obtained at the K point between the second and third bands for $l = 0.31a$ ($<a/3$) and between the first and second bands for $l = 0.35a$ ($>a/3$).

The electric-field distributions of the two bands concerned at K_D are displayed in Fig. 4, which shows that only the resonance modes formed inside the isogonal hexagonal tiles B_1 and B_2 (see Sec. II A) are involved at the Dirac point. It is thus natural that the frequency level of the Dirac point is lowered or raised following l. This is simply because the Dirac point frequency is determined by the frequency level of the resonance mode inside the B tiles that inversely scales with the tile size (see Sec. II C).

C. Tight-binding description

In order to understand the contributions of different local resonance modes in the Dirac cone formation, let us consider the band structures in the framework of a TB model.

A TB description of the EM band structures in similar structures based on local resonance modes inside the structure tiles has previously been discussed [22]. Here we investigate the Dirac cone formation and evolution, and we

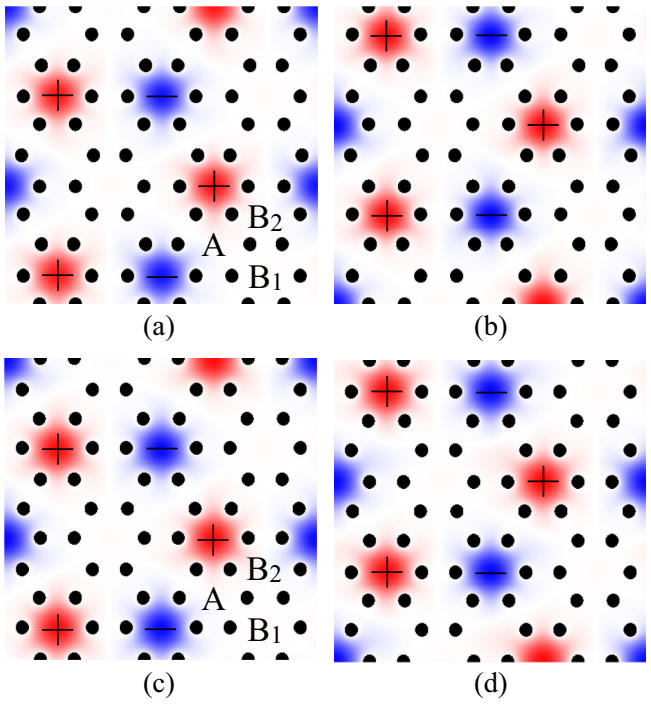

FIG. 4. Electric-field distributions of the two bands involved in the Dirac point for (a) and (b) $l = 0.31a$ and (c) and (d) $l = 0.35a$. The plus and minus signs indicate the polarities.

consider the problem in a more general situation, where the nonorthogonality between local modes should be taken into account to describe the frequency band formation.

Recalling that, in a classical TB model [24], the crystal wave function can be expressed as the sum of local mode wave functions $|\phi_q\rangle$ defined inside individual tiles,

$$|\Psi_{\mathbf{k}}(\mathbf{r})\rangle = \sum_m \frac{e^{i\mathbf{k}\mathbf{R}_m}}{\sqrt{N}} \sum_q b_q(\mathbf{k}) e^{i\mathbf{k}\mathbf{d}_p} |\phi_q(\mathbf{r} - \mathbf{R}_m - \mathbf{d}_q)\rangle, \quad (1)$$

with $\sum_m$ and $\sum_q$ summing, respectively, over the unit cells and over the modes inside the cell. The coefficient b_q gives the amount of the local mode $|\phi_q\rangle$ in the crystal wave function. In the present case, the local modes are the resonance modes formed inside individual A and B_1 (B_2) tiles (see Sec. II A). $|\phi_q\rangle$ corresponds to the electric-field distributions of these modes.

The crystal Hamiltonian can be written as $H = H_0 + \Delta U(\mathbf{r})$, with $H_0 = -\frac{c^2}{\epsilon}\nabla^2$ being the Hamiltonian of an individual local mode and ΔU being the correction due to the interactions with the other modes. c is the light velocity in vacuum. ϵ stands for the dielectric constant of the medium filling the tile. Its value is unity in the present case, where air is chosen as the background.

We define the following terms:

$$\alpha_{pq} = \langle\phi_p|\phi_q\rangle, \quad \beta_q = -\langle\phi_q|\Delta U(\mathbf{r})|\phi_{\mathbf{q}}\rangle,$$
$$\gamma_{pq} = -\langle\phi_p|\Delta U(\mathbf{r})|\phi_q\rangle. \quad (2)$$

The overlap and energy integrals, α_{pq} and γ_{pq}, describe, respectively, the overlap and energy transfer between neighboring modes, while the β_q term describes the energy-level shift of a local mode.

In the present case, due to the low filling rate, and thus the large tile edge openings w_1' (w_1'') and w_2' (w_2''; Fig. 1), the nonorthogonality between local modes cannot simply be neglected, and the overlap integrals should be taken into account to describe the entire band structure. Restraining the integrals α and γ to those between the first-neighbor modes, the crystal eigenfrequencies ω_k are given by the characteristic equation

$$\det\begin{bmatrix} \omega_A^2 - \beta_A - \omega_k^2 & -\xi\left[\gamma_{\mathrm{AB}_1} - \alpha_{\mathrm{AB}_1}\left(\omega_{B_1}^2 - \omega_k^2\right)\right] & -\xi^*\left[\gamma_{\mathrm{AB}_2} - \alpha_{\mathrm{AB}_2}\left(\omega_{B_2}^2 - \omega_k^2\right)\right] \\ -\xi^*\left[\gamma_{\mathrm{AB}_1} - \alpha_{\mathrm{AB}_1}\left(\omega_A^2 - \omega_k^2\right)\right] & \omega_{B_1}^2 - \beta_{B_1} - \omega_k^2 & -\xi\left[\gamma_{B_1B_2} - \alpha_{B_1B_2}\left(\omega_{B_2}^2 - \omega_k^2\right)\right] \\ -\xi\left[\gamma_{\mathrm{AB}_2} - \alpha_{\mathrm{AB}_2}\left(\omega_A^2 - \omega_k^2\right)\right] & -\xi^*\left[\gamma_{B_1B_2} - \alpha_{B_1B_2}\left(\omega_{B_1}^2 - \omega_k^2\right)\right] & \omega_{B_2}^2 - \beta_{B_2} - \omega_k^2 \end{bmatrix} = 0, \quad (3)$$

with

$$\xi = e^{ik_y a/\sqrt{3}} + 2e^{-ik_y a/2\sqrt{3}}\cos(k_x a/2) \quad (4)$$

and ω_A and $\omega_{B_1(B_2)}$ being the eigenfrequencies of the resonance modes in individual A and B_1 (B_2) tiles, $|\phi_A\rangle$ and $|\phi_{B_1(B_2)}\rangle$. As a matter of fact, for symmetry reasons, it is not necessary to distinguish B_1 and B_2 in Eq. (3). They will both be denoted as B in the following.

The eigenfrequencies ω_A and ω_B can be obtained by solving Maxwell's equations using the FDTD method for individual A and B tiles (see Sec. II A). The parameters α, β, and γ can be obtained by fitting Eq. (3) with the FDTD curves. The obtained values are listed in Table I. The same frequency bands calculated with these parameters are also plotted in Fig. 3. All the FDTD curves are well reproduced. Indeed, the band structures are well described by the TB model.

We may observe in Table I the band parameter variations following l. As a matter of fact, for l lower or greater than $a/3$, the tile edge opening between the A and B tiles w_1' (w_1'') is greater or lower than that between neighboring B tiles w_2' (w_2''; see Fig. 1). As the neighbor distance remains unchanged, the correlations between $|\phi_A\rangle$ and $|\phi_B\rangle$, α_{AB} and γ_{AB}, are stronger or weaker than those between neighboring $|\phi_B\rangle$, α_{BB} and γ_{BB}. Concerning the mode frequencies, the size of the A tile is larger or smaller than that of the B tile. As the resonance wavelength scales with the tile size, ω_A is lower or higher than ω_B.

D. Band structures in the vicinity the Dirac point

At the K point, the off-diagonal elements in the matrix of Eq. (3) all vanish. ω_k^2 takes the values $\omega_A^2 - \beta_A$ and $\omega_B^2 - \beta_B$, the latter being a degenerate double root and corresponding to the Dirac point frequency. The Dirac point is determined by only the $|\phi_B\rangle$ modes, without involving $|\phi_A\rangle$. This corroborates the electric-field distributions in Fig. 4.

The TB model allows further investigating the band structures in the vicinity of the Dirac point in the presence of

TABLE I. The local resonance mode energy levels ω^2, overlap integrals α, energy integrals γ, and energy-level shifts β for $l = 0.31a, a/3$, and $0.35a$. All the energy values are normalized according to $(\omega a/2\pi c)^2$.

l/a	ω_A^2	ω_B^2	α_{AB}	α_{BB}	γ_{AB}	γ_{BB}	β_A	β_B
0.31	1.4302	1.6336	0.0362	0.0243	0.0429	0.0289	0.0002	0.0057
1/3	1.5559	1.5559	0.0308	0.0308	0.0373	0.0373	−0.0001	−0.0001
0.35	1.6718	1.5116	0.0285	0.0390	0.0348	0.0443	0.0085	0.0019

$|\phi_A\rangle$. As a matter of fact, for wave vector k in the vicinity of the Dirac vector K_D, ξ is weak, and the contribution of the overlap integrals α to the band structure can be neglected. For simplicity, we define

$$\Delta\omega_{AB}^2 = \left(\omega_A^2 - \beta_A\right) - \left(\omega_B^2 - \beta_B\right) \tag{5}$$

and

$$\Delta E_k = \omega_k^2 - \left(\omega_B^2 - \beta_B\right), \tag{6}$$

where $\Delta\omega_{AB}^2$ represents the energy-level difference between $|\phi_A\rangle$ and $|\phi_B\rangle$ and ΔE_k is the crystal energy level relative to that of $|\phi_B\rangle$.

Equation (3) can be rewritten as

$$\det\begin{bmatrix} \Delta\omega_{AB}^2 - \Delta E_k & -\xi\gamma_{AB} & -\xi^*\gamma_{AB} \\ -\xi^*\gamma_{AB} & -\Delta E_k & -\xi\gamma_{BB} \\ -\xi\gamma_{AB} & -\xi^*\gamma_{BB} & -\Delta E_k \end{bmatrix} = 0, \tag{7}$$

with its polynomial form being

$$\left(\Delta\omega_{AB}^2 - \Delta E_k\right)\left[(\Delta E_k)^2 - |\xi|^2\gamma_{BB}^2\right] + 2|\xi|^2\gamma_{AB}^2\Delta E_k - (\xi^3 + \xi^{*3})\gamma_{AB}^2\gamma_{BB} = 0. \tag{8}$$

For sufficiently weak ξ, the last two terms on the left side of Eq. (8) can be neglected. We get, close to K_D,

$$\omega_k^2 = \omega_A^2 - \beta_A, \omega_B^2 - \beta_B \pm |\xi|\gamma_{BB}. \tag{9}$$

The Dirac band branches close to K_D can be considered to be essentially determined by the correlations between neighboring $|\phi_B\rangle$, with their slopes at K_D determined by γ_{BB} (normalized by $2\omega_B$). The Dirac cones have an isotropic form at K_D.

For k departing from K_D, the last two terms in Eq. (8) become non-negligible. As a matter of fact, these terms lead to band frequency shifts from those of Eq. (9) unless the band branch is not coupled to $|\phi_A\rangle$ (see below). As can be checked in Eq. (8), the sign of the frequency shifts will depend on that of $\Delta\omega_{AB}^2$. For $\Delta\omega_{AB}^2 < 0$ (e.g., $l = 0.31a$), the Dirac band branches will be shifted up, while, in the opposite case (e.g., $l = 0.35a$), they will be shifted down. In fact, the shift direction is in agreement with the perturbation theory that interacting bands repel each other.

The Dirac band shift effect due to the coupling with $|\phi_A\rangle$ is illustrated in Fig. 5, where the Dirac band branches in the vicinity of K_D, along k_{KM} and $k_{K\Gamma}$, calculated using the TB model [Eq. (3)] with α_{AB} and γ_{AB} set to zero, together with the FDTD solutions, are displayed. The FDTD and TB ($\alpha_{AB} = 0$, $\gamma_{AB} = 0$) curves are tangent at K_D, confirming the above discussion concerning the band slopes that are determined by γ_{BB} at K_D. The up- and downshifts of the band branches resulting from the coupling with $|\phi_A\rangle$ for larger Δk can clearly be seen. The shift magnitudes increase following Δk, and the signs of the shifts are also in agreement with the above discussion.

We note that the lower Dirac branches in the k_{KM} direction and the higher branches in the $k_{K\Gamma}$ direction remain unshifted. To further investigate the involvements of $|\phi_A\rangle$ and $|\phi_B\rangle$ in the band formation, let us consider the coefficients $b_q(\mathbf{k})$ in Eq. (1), which give the contribution of each resonance mode to the crystal wave function and can be obtained using the TB model from the matrix in Eq. (3). Considering the $b_q(\mathbf{k})$ values along k_{KM} and $k_{K\Gamma}$ departing from K_D, the absolute $b_q(\mathbf{k})$ values at $\Delta k = 0.01(2\pi/a)$ and $0.1(2\pi/a)$ for the first three bands are listed in Table II. We can see $|q_A| = 0$ for both the lower Dirac branches in the k_{KM} direction and the higher branches in the $k_{K\Gamma}$ direction. Indeed, these branches are formed by only $|\phi_B\rangle$ and are not coupled to $|\phi_A\rangle$. Concerning the other band branches, $|b_A|$ is much weaker than $|b_B|$ at $\Delta k = 0.01(2\pi/a)$. This confirms that the Dirac bands are essentially formed by $|\phi_B\rangle$ close to K_D. For larger Δk, i.e., $\Delta k = 0.1(2\pi/a)$, the $|b_A|$ values increase by one order of magnitude, and the contributions of $|\phi_A\rangle$ to the Dirac band branches are stronger, corroborating the band shift increases.

E. Structure compression effect

Let us consider the Dirac cone evolution in the presence of structure anisotropy in these lattices. We introduce a uniaxial

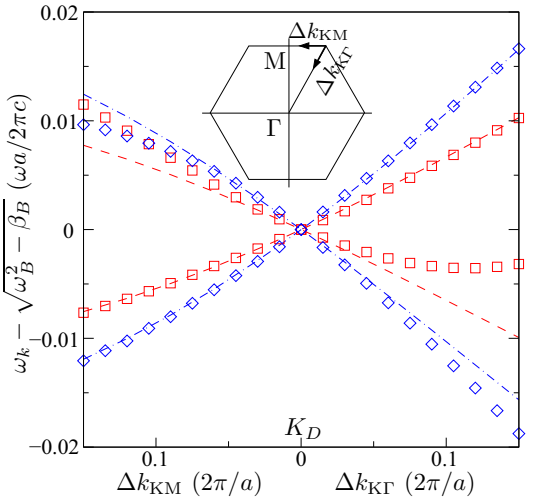

FIG. 5. The Dirac band branches in the vicinity of K_D $(2\pi/3a, 2\pi/\sqrt{3}a)$ along k_{KM} and $k_{K\Gamma}$. The squares and diamonds represent the results obtained with the FDTD method, while the dashed and dash-dotted lines show the curves calculated using the TB model with α_{AB} and γ_{AB} set to zero for $l = 0.31a$ and $l = 0.35a$, respectively. The band frequencies are plotted in $\omega_k - \sqrt{\omega_B^2 - \beta_B}$ for a direct comparison between the two configurations.

TABLE II. The absolute values of the coefficients b_A and b_B of Eq. (1) at different Δk_{KM} and $\Delta k_{\mathrm{K\Gamma}}$ (magnitude in units of $2\pi/a$) for the first three bands for $l = 0.31$ and $0.35a$, obtained from the tight-binding model.

		$\Delta k_{\mathrm{KM}} = 0.01$		$\Delta k_{\mathrm{K\Gamma}} = 0.01$		$\Delta k_{\mathrm{KM}} = 0.1$		$\Delta k_{\mathrm{K\Gamma}} = 0.1$	
l/a	Band	$\lvert b_A\rvert$	$\lvert b_B\rvert$	$\lvert b_A\rvert$	$\lvert b_B\rvert$	$\lvert b_A\rvert$	$\lvert b_B\rvert$	$\lvert b_A\rvert$	$\lvert b_B\rvert$
0.31	First	0.9999	0.0116	0.9999	0.0119	0.9906	0.0967	0.9831	0.1293
	Second	0	0.7071	0.0168	0.7070	0	0.7071	0.1821	0.6953
	Third	0.0163	0.7070	0	0.7071	0.1361	0.7005	0	0.7071
0.35	First	0	0.7071	0.0172	0.7070	0	0.7071	0.1517	0.6989
	Second	0.0175	0.7070	0	0.7071	0.1759	0.6961	0	0.7071
	Third	0.9998	0.0123	0.9999	0.0121	0.9845	0.1239	0.9886	0.1065

compression along the y axis by reducing the height of the unit cell by a factor δ. It is known [25,26] that, in atomic structures, anisotropy in the neighbor-site interactions leads to Dirac cone anisotropy and Dirac point shift and, eventually, to Dirac point merging and an energy gap opening. The anisotropy is reinforced in the metallic triangular lattice [20]. We show here that, in these isogonal structures, the Dirac cones undergo anisotropic deformation due to not only the anisotropy in the correlations between neighboring $|\phi_B\rangle$ but also that between $|\phi_A\rangle$ and $|\phi_B\rangle$ when departing from K_D. Both these anisotropies are reinforced by the metallic nature of the lattice.

The $\xi\gamma$ and $\xi\alpha$ terms in Eq. (3) should be replaced in the presence of the deformation field by $\zeta\gamma' + \eta\gamma''$ and $\zeta\alpha' + \eta\alpha''$, with

$$\begin{aligned} \zeta &= e^{ik_y a(1-\delta)/\sqrt{3}}, \\ \eta &= 2e^{-ik_y a(1-\delta)/2\sqrt{3}}\cos(k_x a/2), \end{aligned} \tag{10}$$

γ' and α' representing the integrals along y and γ'' and α'' representing those in the other directions.

The band diagrams for $\delta = 0.05$, 0.10, and 0.15 for $l = 0.31a$ and $l = 0.35a$, obtained using the FDTD method, are displayed in Figs. 6 and 7. The band parameters, obtained by fitting these curves using the TB model and taking into account the relations in Eq. (10), with ω_A and ω_B obtained with the FDTD method for deformed individual tiles, are shown in Table III and Fig. 8. The frequency bands calculated with these parameters are plotted together with the FDTD curves in the same figures. Again, the band structures are well reproduced by the TB model. The Dirac points K_D are shifted towards the M point following the structure compression. We note that, for $l = 0.31a$ (Fig. 6), the Dirac point merging does not lead to a gap opening between the second and third bands due to the upshift of the second band along the $\Gamma - K$ and $M - \Gamma$ paths, resulting from the coupling with $|\phi_A\rangle$.

Let us consider again the band structures in the vicinity of K_D. Taking into account Eq. (10), the polynomial equation (8)

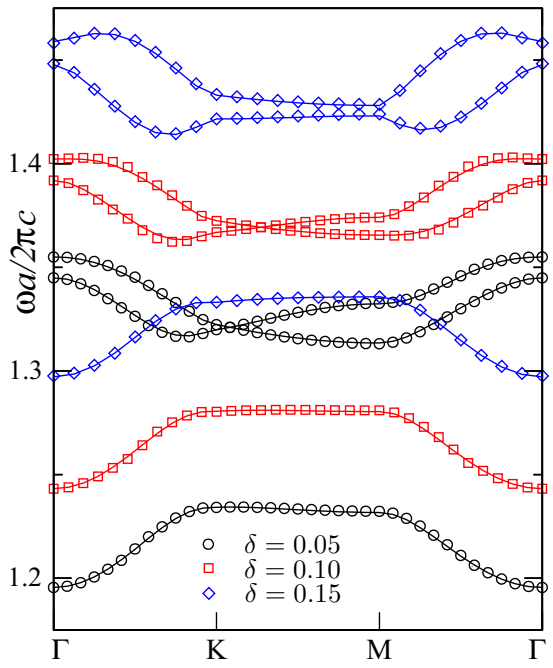

FIG. 6. The first three bands for $l = 0.31a$ following the structure compression δ. The FDTD solutions are represented by various symbols, while those obtained with the tight-binding model are shown by solid lines.

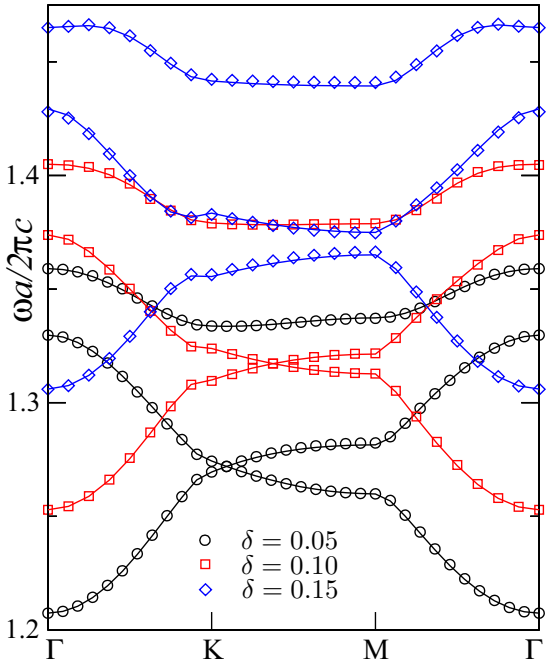

FIG. 7. The first three bands for $l = 0.35a$ following the structure compression δ. The FDTD solutions are represented by various symbols, while those obtained with the tight-binding model are shown by solid lines.

TABLE III. The local resonance mode energy levels ω^2 and energy-level shifts β for $l = 0.31a$ and $0.35a$, following the compression factor δ. All the values are normalized according to $(\omega a/2\pi c)^2$.

	$l = 0.31a$			$l = 0.35a$		
	$\delta = 0.05$	$\delta = 0.10$	$\delta = 0.15$	$\delta = 0.05$	$\delta = 0.10$	$\delta = 0.15$
ω_A^2	1.5289	1.6489	1.7719	1.7866	1.9192	2.0635
ω_B^2	1.7475	1.8783	2.0273	1.6195	1.7414	1.8787
β_A	0.0055	0.0077	−0.0135	0.0081	0.0196	−0.0072
β_B	0.0024	0.0032	−0.0045	0.0017	0.0064	0.0015

will take the following form:

$$\begin{aligned}&\left(\Delta\omega_{\rm AB}^2-\Delta E_k\right)[(\Delta E_k)^2-(\zeta\gamma'_{\rm BB}+\eta\gamma'_{\rm BB})(\zeta^*\gamma'_{\rm BB}+\eta^*\gamma''_{\rm BB})]\\&+2(\zeta\gamma'_{\rm AB}+\eta\gamma''_{\rm AB})(\zeta^*\gamma'_{\rm AB}+\eta^*\gamma''_{\rm AB})\Delta E_k\\&-[(\zeta\gamma'_{\rm AB}+\eta\gamma''_{\rm AB})^2(\zeta\gamma'_{\rm BB}+\eta\gamma''_{\rm BB})+(\zeta^*\gamma'_{\rm AB}+\eta^*\gamma''_{\rm AB})^2\\&\times(\zeta^*\gamma'_{\rm BB}+\eta^*\gamma''_{\rm BB})]=0.\end{aligned}\tag{11}$$

For k close to K_D, the terms from the second to fourth lines in Eq. (11) can be neglected. We get

$$\begin{aligned}\omega_k^2&=\omega_A^2-\beta_A,\\\omega_B^2-\beta_B&\pm\sqrt{(\zeta\gamma'_{\rm BB}+\eta\gamma'_{\rm BB})(\zeta^*\gamma'_{\rm BB}+\eta^*\gamma''_{\rm BB})}.\end{aligned}\tag{12}$$

The Dirac cone is anisotropic at K_D due to the anisotropy in the correlations between $|\phi_B\rangle$. This is similar to the cases discussed in Refs. [25,26], with the particularity that, in the present case, $\gamma'_{\rm BB}$ increases while $\gamma''_{\rm BB}$ decreases following the structure deformation, as shown in Fig. 8.

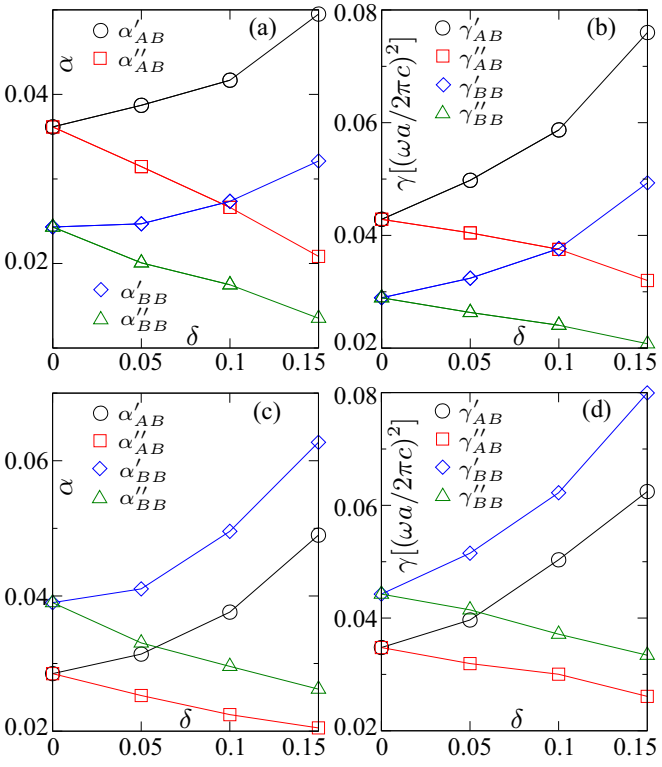

FIG. 8. The variation of the overlap and energy integrals along the compression axis y (α' and γ') and in the other two directions (α'' and γ'') following the deformation factor δ for (a) and (b) $l = 0.31a$ and (c) and (d) $l = 0.35a$. The solid lines are guides to the eye.

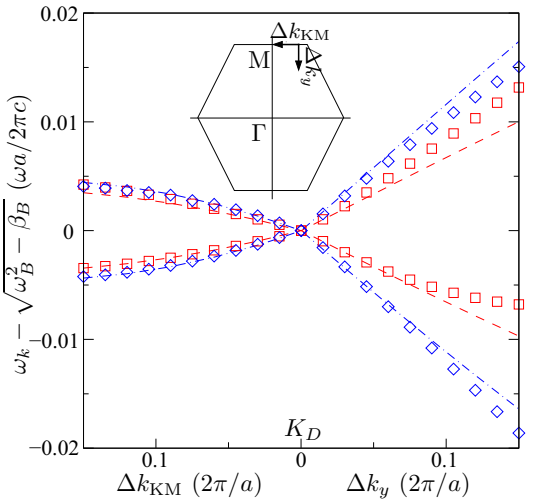

FIG. 9. The Dirac band branches in the vicinity of K_D along $k_{\rm KM}$ and k_y in the presence of a compression deformation of $\delta = 0.10$. The squares and diamonds represent the results obtained with the FDTD method, while the dashed and dash-dotted lines show the curves calculated using the TB model with $\alpha'_{\rm AB}$, $\alpha''_{\rm AB}$, $\gamma'_{\rm AB}$, and $\gamma''_{\rm AB}$ all set to zero for $l = 0.31a$ and $l = 0.35a$, respectively. The band frequencies are plotted in $\omega_k - \sqrt{\omega_B^2 - \beta_B}$ for a direct comparison between the two configurations.

For k departing from K_D, the last two terms in Eq. (11) lead to band frequency shifts from those of Eq. (12). This is illustrated in Fig. 9, where the Dirac band branches for $\delta = 0.10$ in the vicinity of K_D and along $k_{\rm KM}$ and k_y, calculated using the TB model with $\alpha'_{\rm AB}$ and $\alpha''_{\rm AB}$ and $\gamma'_{\rm AB}$ and $\gamma''_{\rm AB}$ set to zero, are displayed together with the FDTD solutions. It is obvious that the Dirac cone, becoming anisotropic due to the anisotropic correlations between neighboring $|\phi_B\rangle$, undergoes further band shifts for increasing Δk, and the shifts are much stronger along k_y than along $k_{\rm KM}$. This can be related to the increasing $\gamma'_{\rm AB}$ and decreasing $\gamma''_{\rm AB}$ following the structure deformation (Fig. 8).

The above results can be compared to Table IV, in which the absolute $b_q(\mathbf{k})$ values for $\delta = 0.10$ obtained using the TB model are listed. It shows that, like for the undeformed structures, the Dirac band branches close to K_D are essentially determined by $|\phi_B\rangle$, with the contribution of $|\phi_A\rangle$ being weak; however, for larger Δk, the contributions of $|\phi_A\rangle$ become much stronger. Moreover, for the same magnitude of Δk, the contributions of $|\phi_A\rangle$ are much stronger along k_y than along $k_{\rm KM}$. In addition, like for the undeformed structures, the lower Dirac band branches along $k_{\rm KM}$ are not coupled to $|\phi_A\rangle$.

The anisotropies, both at K_D and when departing from the K_D point, are reinforced by the metallic nature of the lattice. Indeed, as shown in Fig. 8, the mode correlations along the y axis, $\alpha'_{\rm AB}$ and $\gamma'_{\rm AB}$ and $\alpha'_{\rm BB}$ and $\gamma'_{\rm BB}$, increase while those in the other directions, $\alpha''_{\rm AB}$ and $\gamma''_{\rm AB}$ and $\alpha''_{\rm BB}$ and $\gamma''_{\rm BB}$, decrease following the deformation factor δ. This confirms the phenomenon obtained for the triangular structure [20]. The neighbor-mode correlations depend on the neighbor distance

TABLE IV. The absolute values of the coefficients b_A and b_B of Eq. (1) at different $\Delta k_{\rm KM}$ and Δk_y (magnitude in units of $2\pi/a$) for the first three bands for $l = 0.31$ and $0.35a$ under a compression deformation of $\delta = 0.10$, obtained with the tight-binding model.

		$\Delta k_{\rm KM} = 0.01$		$\Delta k_y = 0.01$		$\Delta k_{\rm KM} = 0.1$		$\Delta k_y = 0.1$	
l/a	Band	$\lvert b_A\rvert$	$\lvert b_B\rvert$	$\lvert b_A\rvert$	$\lvert b_B\rvert$	$\lvert b_A\rvert$	$\lvert b_B\rvert$	$\lvert b_A\rvert$	$\lvert b_B\rvert$
0.31	First	1.0000	0.0061	0.9999	0.0122	0.9977	0.0476	0.9859	0.1185
	Second	0	0.7071	0.0124	0.7071	0	0.7071	0.1272	0.7014
	Third	0.0087	0.7071	0.0122	0.7071	0.0675	0.7055	0.1099	0.7028
0.35	First	0	0.7071	0.0148	0.7070	0	0.7071	0.1368	0.7005
	Second	0.0087	0.7071	0.0149	0.7070	0.0697	0.7054	0.1441	0.6997
	Third	1.0000	0.0061	0.9998	0.0147	0.9976	0.0488	0.9804	0.1392

and, in a metallic lattice, the edge opening between neighboring tiles. In the present case, the neighbor distances are reduced by the factor δ along the y axis, while the corresponding edge lengths, and thus the edge openings, e.g., w_1' and w_2' in Fig. 1, remain unchanged. In the other directions, the neighbor distances are reduced by a factor of about $\frac{1}{2}\delta\sin(\pi/6)$, while the corresponding edge lengths are more strongly reduced by a factor of about $\frac{\sqrt{3}}{2}\delta\cos(\pi/6)$. The reductions of the corresponding edge openings, e.g., w_1'' and w_2'' in Fig. 1, are still stronger due to the nonzero cylinder radius r. Therefore, the neighbor-mode correlations increase along the compression axis and decrease along the other directions.

III. DISCUSSION

As discussed in Sec. II D, the correlations between different neighbor modes have different consequences on the shape of the Dirac cones. In fact, Dirac cones are obtained for $\Delta\omega_{\rm AB}^2 \neq 0$, with their slope at K_D determined by the energy integral $\gamma_{\rm BB}$ between neighboring modes $|\phi_B\rangle$. Let us further consider the role played by the energy integral and the energy-level difference between modes $|\phi_A\rangle$ and $|\phi_B\rangle$, $\gamma_{\rm AB}$ and $\Delta\omega_{\rm AB}^2$, on the band shifts departing from K_D.

The analytical solution of Eq. (8) is tedious. However, the roots have simple forms along certain high-symmetry axes. As a matter of fact, we get along $k_{\rm KM}$

$$\begin{aligned}\omega_k^2 &= \omega_A^2 - \beta_A + \delta\omega_k^2,\\ &= \omega_B^2 - \beta_B + |\xi|\gamma_{\rm BB} - \delta\omega_k^2,\\ &= \omega_B^2 - \beta_B - |\xi|\gamma_{\rm BB}\end{aligned} \tag{13}$$

and along $k_{\rm K\Gamma}$

$$\begin{aligned}\omega_k^2 &= \omega_A^2 - \beta_A + \delta\omega_k^2,\\ &= \omega_B^2 - \beta_B + |\xi|\gamma_{\rm BB},\\ &= \omega_B^2 - \beta_B - |\xi|\gamma_{\rm BB} - \delta\omega_k^2,\end{aligned} \tag{14}$$

where

$$\delta\omega_k^2 = \frac{1}{2}\Big[-\left(\Delta\omega_{\rm AB}^2 \mp |\xi|\gamma_{\rm BB}\right) \pm\sqrt{\left(\Delta\omega_{\rm AB}^2 \mp |\xi|\gamma_{\rm BB}\right)^2 + 8|\xi|^2\gamma_{\rm AB}^2}\Big], \tag{15}$$

with $\mp$ for the $k_{\rm KM}$ and $k_{\rm K\Gamma}$ directions and $\pm$ for $\Delta\omega_{\rm AB}^2 > 0$ and < 0. In fact, Eqs. (13) and (14) yield the maximum ($\delta\omega_k^2$) and minimum (zero) shift magnitudes for the Dirac cone and also confirm that $|\phi_A\rangle$ is not involved in the formation of the lower Dirac band branch along $k_{\rm KM}$ and the higher branch along $k_{\rm K\Gamma}$.

For k close to K_D, Eq. (15) takes the approximative form

$$\delta\omega_k^2 \approx \frac{2|\xi|^2\gamma_{\rm AB}^2}{\Delta\omega_{\rm AB}^2 \mp |\xi|\gamma_{\rm BB}}, \tag{16}$$

with $\mp$ for the $k_{\rm KM}$ and $k_{\rm K\Gamma}$ directions. And the corresponding frequency band branches can be expressed as

$$\omega_k \approx \omega_B - \frac{1}{\omega_B}\left(\frac{\beta}{2} \mp \frac{\gamma_{\rm BB}}{2}|\xi| + \frac{\gamma_{\rm AB}^2}{\Delta\omega_{\rm AB}^2}|\xi|^2\right), \tag{17}$$

with $\mp$ for the upper branch along $k_{\rm KM}$ and the lower branch along the $k_{\rm K\Gamma}$ direction. The frequency band shifts are quadratic in $|\xi|$, deviating from the linear relation in $|\xi|$ at K_D. The shift magnitude scales with the ratio $\gamma_{\rm AB}^2/\Delta\omega_{\rm AB}^2$.

It is possible to modulate the Dirac cone shape through the common edge length l between neighbor isogonal tiles without modifying the lattice periodicity and breaking the structure symmetry. On the one hand, by varying l, we can modulate the edge opening between the tiles, w_1' (w_1'') and w_2' (w_2''). This allows controlling $\gamma_{\rm AB}$ and $\gamma_{\rm BB}$. On the other hand, since the resonance mode frequency inside a tile scales inversely with the tile size, the l variation allows us to modulate the relative frequency levels of $|\phi_A\rangle$ and $|\phi_B\rangle$, thus controlling the energy-level difference $\Delta\omega_{\rm AB}^2$.

The Dirac cone structures for $l = 0.31a$ and $0.35a$ already provide an example, in particular concerning the band slopes at K_D and the band shift directions when departing from K_D. Here we further illustrate the cone variations, especially in relation to $\gamma_{\rm AB}$ and $\Delta\omega_{\rm AB}^2$. Consider the cases of $l = 0.32a$ and $0.34a$. As compared to the cases of $l = 0.31a$ and $0.35a$, respectively, the edge openings w_1' (w_1'') and w_2' (w_2''), as well as the sizes of the A and B tiles, are closer to each other in each configuration. Following the procedure described in Sec. II, we get the TB model band parameters that are listed in Table V. Notably, compared to those in Table I, in each configuration, the values of $\gamma_{\rm AB}$ and $\gamma_{\rm BB}$, as well as those of ω_A^2 and ω_B^2, are closer to each other (as a matter of fact, they all tend to the values for $l = a/3$ given in Table I). The magnitudes of $\Delta\omega_{\rm AB}^2$ are reduced so that those of the $\gamma_{\rm AB}^2/\Delta\omega_{\rm AB}^2$ ratios increase, the latter changing from -0.0093 and 0.0079 $[(\omega a/2\pi c)^2]$ for $l = 0.31a$ and $0.35a$ to -0.0129 and 0.0232 $[(\omega a/2\pi c)^2]$ for $l = 0.32a$ and $0.34a$. Consequently, the Dirac cone slope at K_D will increase for $l = 0.32$ and decrease for $l = 0.34$ compared to $l = 0.31a$ and $0.35a$, respectively, and the band shifts due to the correlations between $|\phi_A\rangle$ and $|\phi_B\rangle$ will increase in both

TABLE V. The local mode energy levels ω^2, overlap integrals α, energy integrals γ, and energy-level shifts β for $l = 0.32a$ and $0.34a$. All the energy values are normalized according to $(\omega a/2\pi c)^2$.

l/a	ω_A^2	ω_B^2	α_{AB}	α_{BB}	γ_{AB}	γ_{BB}	β_A	β_B
0.32	1.4759	1.6006	0.0331	0.0252	0.0404	0.0316	0.0008	−0.0016
0.34	1.6035	1.5395	0.0297	0.0326	0.0361	0.0401	0.0056	−0.0023

cases. The Dirac band branches in the vicinity of K_D for these two configurations, calculated using the TB model [Eq. (3)] with α_{AB} and γ_{AB} set to zero, are plotted in Fig. 10, together with the FDTD solutions. Compared to those in Fig. 5, the variations predicted above can clearly be seen.

Finally, as the upper and lower Dirac band branches are shifted in the same direction for a given $\Delta\omega_{AB}^2$ value, with different shift magnitude distributions following the k direction, the Dirac cone deformation due to the coupling with $|\phi_A\rangle$ breaks the mirror symmetry between the upper and lower parts in the vicinity of K_D implied by Eq. (9), where only the correlations between neighboring $|\phi_B\rangle$ are taken into account. The cone still displays, however, a threefold rotational symmetry.

Indeed, the symmetry of the cone is imposed by the local symmetry in the crystals and, in the TB model, by the characteristic equation [Eq. (3)], where the parameter ξ [Eq. (4)] has threefold symmetry. The roots of Eqs. (13) and (14), as well as the frequency band shifts in Fig. 10, are, in fact, distributed modulo $2\pi/3$ following k orientation. Indeed, the threefold symmetry is well illustrated by the isofrequency lines obtained from Eq. (3), displayed in Fig. 11, which shows, moreover, that, for both the up- and downshifts, the maxima and the minima (zero) of the shift magnitude are distributed along k_{KM} and $k_{K\Gamma}$ modulo $2\pi/3$ for the upper part of the cone; however, for the lower part, the maxima and the minima (zero) of the shift magnitude are distributed along $k_{K\Gamma}$ and k_{KM} modulo $2\pi/3$.

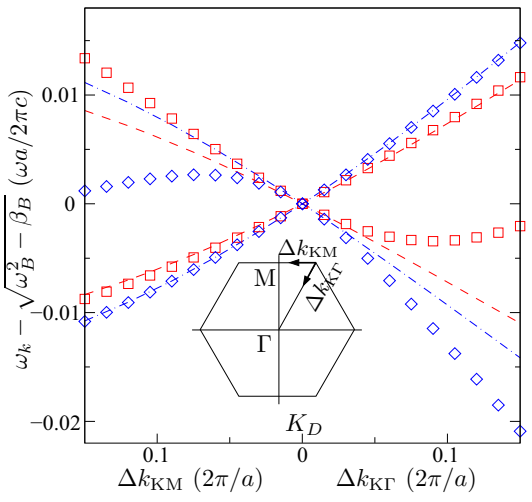

FIG. 10. The Dirac band branches in the vicinity of K_D $(2\pi/3a, 2\pi/\sqrt{3}a)$ along k_{KM} and $k_{K\Gamma}$. The squares and diamonds represent the results obtained with the FDTD method, while the dashed and dash-dotted lines show the curves calculated using the TB model with α_{AB} and γ_{AB} set to zero for $l = 0.32a$ and $l = 0.34a$, respectively. The band frequencies are plotted in $\omega_k - \sqrt{\omega_B^2 - \beta_B}$ for a direct comparison between the two configurations.

The trigonal deformation of the Dirac cone, as illustrated in Fig. 11, leads to anisotropies in the group velocity and the refraction index and directly impacts the EM wave dynamics in the vicinity of the Dirac point. By adjusting the l value that allows modulating the orientation and the magnitude of the cone deformation, it will be possible to control the wave propagation and, in particular, trigger the polarized EM beam propagation [27] and alter the conical diffraction [14]. To the best of our knowledge, these phenomena have not yet been reported for metallic structures.

As a matter of fact, the trigonal deformation breaks the valley degeneracy around two inequivalent Dirac points (K and K') and can lead to valley-polarized EM beam propagation. We can observe beam splitting along the y axis (the armchair orientation) and collimation along the x axis (the zigzag orientation) for both $l < a/3$ and $l > a/3$. The frequency level at which the beam polarization occurs relative to the Dirac point frequency can be adjusted through the l value. Concerning the conical diffraction, for l close to $a/3$, the diffraction rings will undergo trigonal distortion, with opposite orientations for $l < a/3$ and $l > a/3$ around the same Dirac point. Moreover, given

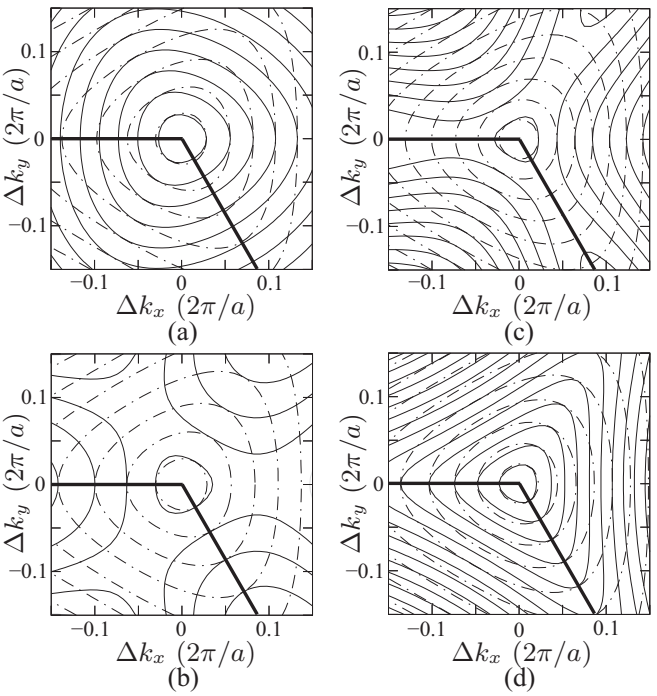

FIG. 11. Isofrequency lines (solid lines) for the Dirac cones in the vicinity of K_D $(2\pi/3a, 2\pi/\sqrt{3}a)$, with (a) the upper and (b) lower parts for $l = 0.32a$ and (c) the upper and (d) lower parts for $l = 0.34a$. The dash-dotted lines represent the curves calculated with α_{AB} and γ_{AB} set to zero. The thick lines represent the first Brillouin zone boundaries.

sufficient evolution time, the diffraction rings will be doubled if those associated with both the upper and lower parts of the cone are excited. In fact, rings associated with the upper part will propagate faster than those associated with the lower part for $l < a/3$ and vice versa for $l > a/3$. These phenomena can be checked by measuring the wave transport for different l values.

It is useful to point out that the mechanism described in the present work, based on the resonance modes confined inside the tiles, is valid for only the low-frequency EM bands with TM polarization. In fact, TM waves can couple to longitudinal charge oscillations along the metallic cylinder axis and lead to resonance modes inside the tiles with vanishing electric field at the cylinder surface. In addition, the bands considered in the present work are the lowest-frequency ones, formed by the lowest-frequency resonance modes, similar to the TM_{01} mode in a cylindrical cavity. Higher-order modes can also be confined in the tiles and form Dirac singularities but at higher frequency levels. In a general way, higher-frequency bands, with shorter wavelengths, tend to involve spatially more extended modes and can no longer be well described in terms of local resonance correlations. Concerning the TE polarization (magnetic field perpendicular to the lattice plane), TE waves cannot couple to longitudinal charge oscillations, and at low filling rate, the TE band structures remain similar to those of the free space. Surface plasmon modes, associated with individual cylinders, can be excited and form flat bands, but only in the frequency range close to the surface plasmon frequency of the metal material [28,29].

In practice, for experiments in the microwave range, a lattice with $a = 20$ mm and $l = 7$ mm ($= 0.35a$) will yield a Dirac frequency of about 18.5 GHz. Such structures can easily be fabricated mechanically. For the near-infrared range, the geometrical parameters will scale down to the micron or submicron range, and more demanding lithographic patterning techniques will be needed.

IV. CONCLUSION

In summary, we studied the low-frequency EM band structures in honeycomb-related isogonal hexagonal metallic lattices containing two kinds of tiles, the regular hexagonal ones and the isogonal hexagonal ones, using the FDTD method and in the framework of a TB model. Contrary to a regular honeycomb metallic lattice, an isogonal hexagonal one can generate Dirac cones in its spectrum that are determined by the correlations between the resonance modes formed inside the isogonal hexagonal tiles and have isotropic slope at the Dirac points. The Dirac band branches are, however, shifted in frequency following wave vectors departing from the Dirac points due to the correlations with the resonance modes sustained by the hexagonal tiles, inducing nonlinear trigonal deformation of the Dirac cones. The Dirac cone evolution under structure deformation is also affected by the modes inside the hexagonal tiles since the structure deformation induces anisotropy not only in the mode correlations between the isogonal tiles but also in that between the isogonal and hexagonal tiles. Both these anisotropies are reinforced by the lattice's metallic nature. An isogonal hexagonal lattice provides more degrees of freedom for tuning the Dirac cone shape, which can be adjusted, without altering the lattice periodicity and symmetry by adjusting the structure configuration at local scale and thus modulating the resonance mode correlations.

[1] M. Polini, F. Guinea, M. Lewenstein, H. C. Manoharan, and V. Pellegrini, Nat. Nanotechnol. **8**, 625 (2013).

[2] G. De Simoni, A. Singha, M. Gibertini, B. Karmakar, M. Polini, V. Piazza, L. N. Pfeiffer, K. W. West, F. Beltram, and V. Pellegrini, Appl. Phys. Lett. **97**, 132113 (2010).

[3] K. K. Gomes, W. Mar, W. Ko, F. Guinea, and H. C. Manoharan, Nature (London) **483**, 306 (2012).

[4] P. Soltan-Panahi, J. Struck, P. Hauke, A. Bick, W. Plenkers, G. Meineke, C. Becker, P. Windpassinger, M. Lewenstein, and K. Sengstock, Nat. Phys. **7**, 434 (2011).

[5] L. Tarruell, D. Greif, T. Uehlinger, G. Jotzu, and T. Esslinger, Nature (London) **483**, 302 (2012).

[6] T. Jacqmin, I. Carusotto, I. Sagnes, M. Abbarchi, D. D. Solnyshkov, G. Malpuech, E. Galopin, A. Lemaître, J. Bloch, and A. Amo, Phys. Rev. Lett. **112**, 116402 (2014).

[7] M. Schmidt, V. Peano, and F. Marquardt, New. J. Phys. **17**, 023025 (2015).

[8] F. D. M. Haldane and S. Raghu, Phys. Rev. Lett. **100**, 013904 (2008).

[9] T. Ochiai and M. Onoda, Phys. Rev. B **80**, 155103 (2009).

[10] X. Zhang and Z. Liu, Phys. Rev. Lett. **101**, 264303 (2008).

[11] D. Torrent and J. Sánchez-Dehesa, Phys. Rev. Lett. **108**, 174301 (2012).

[12] G. Weick, C. Woollacott, W. L. Barnes, O. Hess, and E. Mariani, Phys. Rev. Lett. **110**, 106801 (2013).

[13] G. Weick and E. Mariani, Eur. Phys. J. B **88**, 1 (2015).

[14] O. Peleg, G. Bartal, B. Freedman, O. Manela, M. Segev, and D. N. Christodoulides, Phys. Rev. Lett. **98**, 103901 (2007).

[15] R. A. Sepkhanov, Ya. B. Bazaliy, and C. W. J. Beenakker, Phys. Rev. A **75**, 063813 (2007).

[16] S. Raghu and F. D. M. Haldane, Phys. Rev. A **78**, 033834 (2008).

[17] X. Huang, Y. Lai, Z. H. Hang, H. Zheng, and C. T. Chan, Nat. Mater. **10**, 582 (2011).

[18] M. Plihal and A. A. Maradudin, Phys. Rev. B **44**, 8565 (1991).

[19] S. Bittner, B. Dietz, M. Miski-Oglu, P. Oria Iriarte, A. Richter, and F. Schäfer, Phys. Rev. B **82**, 014301 (2010).

[20] K. Wang, Mater. Res. Express **3**, 115007 (2016).

[21] K. Wang, Phys. Rev. B **86**, 235110 (2012).

[22] K. Wang, J. Opt. Soc. Am. B **31**, 1273 (2014).

[23] B. Grünbaum, and G. C. Shephard, Trans. Am. Math. Soc. **242**, 335 (1978).

[24] See, for example, N. W. Ashcroft and N. D. Mermin, *Solid State Physics* (Saunders College, Philadelphia, 1976), Chap. 10.

[25] Y. Hasegawa, R. Konno, H. Nakano, and M. Kohmoto, Phys. Rev. B **74**, 033413 (2006).

[26] J. Feilhauer, W. Apel, and L. Schweitzer, Phys. Rev. B **92**, 245424 (2015).

[27] J. L. Garcia-Pomar, A. Cortijo, and M. Nieto-Vesperinas, Phys. Rev. Lett. **100**, 236801 (2008).

[28] V. Kuzmiak, A. A. Maradudin, and F. Pincemin, Phys. Rev. B **50**, 16835 (1994).

[29] T. Ito and K. Sakoda, Phys. Rev. B **64**, 045117 (2001).